Towards Flapping Wing Control for a Micromechanical Flying Insect *

J. Yan   R.J. Wood   S. Avadhanula   D. Campolo   M. Sitti   R.S. Fearing

Dept of EECS, University of California, Berkeley, CA 94720
{*joeyan, rjwood, srinath, minmo, sitti, ronf*} *@robotics.eecs.berkeley.edu*

Abstract

There has been much progress in the development of the micromechanical flying insect. Flexure joint lifetime has been extended to over 10^6 cyles. Miniature piezoelectric PZn-PT unimorph actuators were fabricated and used to drive a four-bar transmission mechanism. The current thorax design utilizes two actuated four-bars and a spherical joint to drive a rigid wing. Wing forces were measured using strain gauges. These forces can be used for closed-loop wing control.

1 Introduction

Micro aerial vehicles (MAVs) have attained a great deal of attention in the past decade due to favorable feasibility studies. Commercial and military applications for such robotic devices have been identified including operations in hazardous environments (*e.g.,* search-and-rescue within collapsed buildings, nuclear plant exploration in a radiation leak, *etc.*) and defense-related missions (*e.g.,* reconnaissance and surveillance).

Although several groups have worked on MAVs based on fixed or rotary wings (*e.g.* [10]), flapping flight provides superior maneuverability which would be beneficial in obstacle avoidance and necessary for navigation in small spaces, as demonstrated by biological flying insects. It has long been known that insect flight cannot be explained by steady state aerodynamics and only in recent years has there been elucidation of the unsteady aerodynamic mechanisms which account for the large lift forces generated. *Delayed stall* was identified by Ellington *et al* as an important translational means of achieving high lift forces [5]. Dickinson *et al* observed that this phenomenon was inadequate in accounting for the total lift and, using a dynamically-scaled model of a fruit fly, established two additional important lift mechanisms: *rotational*

circulation and *wake capture* [4]. The success of flapping MAVs depends on exploitation of all three mechanisms.

Shimoyama pioneered work in micro-robotic flight ([13], [9]) while milli-robotic flapping flight has been pursued by several other groups ([3], [11]). Early work on the UC Berkeley micromechanical flying insect (MFI) was described by Fearing *et al* in [7] while some of the basic thorax fabrication techniques were presented by Shimada *et al* in [12].

This paper describes progress in the areas of mechanical design and fabrication, actuation and sensing, and control for the MFI.

2 Design

Figure 1 illustrates the design of the MFI. The design specifications, as outlined in [7], are summarized as follows: $100mg$ mass, $25mm$ wingspan, $150Hz$ wingbeat frequency, $8mW$ of mechanical power delivered to both wings, and each wing must independently have 140° flapping range and 90° rotation range (these last two requirements, coupled with the bandwidth, are necessary to exploit the unsteady aerodynamic mechanisms described in section 1).

Figure 1: (a) Conceptual drawing of MFI; (b) Preassembled view showing modular components

2.1 Actuation

2.1.1 Flexure Design and Fabrication

The target operating time for the MFI is roughly 10 minutes, which at $150Hz$, is equivalent to 10^5 cyles.

The flexures are likely failure points and must be designed to endure this level of fatigue stress; this can be done by ensuring that material yielding does not occur.

The fatigue-testing apparatus in figure 2(a) uses a rod on a voice coil actuator (VCA) to cyclically stress one surface of a flexure between zero and some maximum value. Preliminary testing demonstrated that steel flexures would not survive the required level of cyclic stresses (see figure 2(b)) so they were replaced with polyester flexures. The following analysis explains their superior performance.
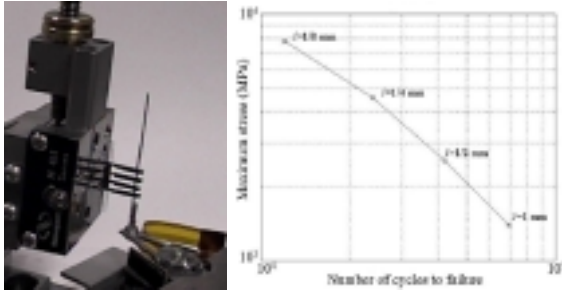

Figure 2: (a) Fatigue testing apparatus; (b) Results using steel flexures of lengths from $\frac{1}{8}mm$ to $1mm$.

The flexures permit the desired rotational compliance between two links but also unwanted translational compliance. By making the flexure length, l, smaller, they can better simulate ideal pin joints. Unfortunately, shorter flexures also result in higher induced stresses for a given joint angle, restricting the minimum flexure lengths. For a beam section of thickness t, bent into a circular arc of radius ρ and made of a material with Young's modulus E, Poisson ratio ν and yield stress S_Y, the maximum stress σ_{max} occurs at the surface:

$$\sigma_{max} = \frac{Et}{2(1-\nu^2)\rho} \qquad (1)$$

Assuming the von Mises yield criterion in which plastic deformation occurs when $\sigma_{max} = \frac{S_Y}{\sqrt{1-\nu+\nu^2}}$, the corresponding radius ρ_Y at which yielding occurs is found to be:

$$\rho_Y = \frac{Et\sqrt{1-\nu+\nu^2}}{2(1-\nu^2)S_Y} = \frac{t\sqrt{1-\nu+\nu^2}}{2(1-\nu^2)\epsilon_Y} \qquad (2)$$

For nonlinear materials, the latter part of the equation using the yield strain ϵ_Y is more appropriate.

Consider figure 3 in which the flexure connects two links at an angle θ. The flexure angle is $\alpha = \pi - \theta = l/\rho$. Given a minimum angle θ, the minimum flexure
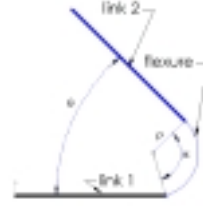
Figure 3: Flexure stress analysis

length is:

$$l_{min} = \rho_Y\alpha = \frac{t(\pi-\theta)\sqrt{1-\nu+\nu^2}}{2(1-\nu^2)\epsilon_Y} \qquad (3)$$

According to this equation, an AISI 302 stainless steel flexure having $\epsilon_Y = 0.14\%$, $t = 12.5\mu m$ and experiencing an angle of $\theta = 40^o$, would need to be at least $l_{min} = 10.3mm$ long to avoid yielding. Replacing this with a polyester flexure having $\epsilon_Y = 4\%$, the flexure would only need to be $l_{min} = 0.38mm$ long. This is a conservative estimate because some level of yielding is permitted. In fact, polyester flexures as short as $0.125mm$ in length were tested using the fatigue apparatus and they all lasted over 10^6 cycles. From this study, it is clear that polymers or other materials which have a high yield strain are required for these flexures.

Getting good adhesion between the polyester flexures and the steel links has been difficult and *peeling* of the flexure away from the steel surface during actuation was a significant problem. Cyanoacrylate adhesives bond well to steel so one solution is to employ steel plates on either side of the polyester to "sandwich" the flexure. Although this method has been successful, it adds an additional level of complexity to the template design and assembly stage. The use of MEMS to fabricate polyimide flexures, as done by Suzuki *et al* in [14], is also being pursued.

2.1.2 Four-bar Kinematics

The basic mechanical transmission element in this design is the four-bar mechanism. Figure 4 illustrates an early cable-driven design in which lateral actuation of the piezo tip P_2 in one direction causes tension on one side of cable C_1C_2, resulting in a net rotation of the wing spar. The structure was fabricated and driven by the final-sized PZn-PT unimorph actuator at a frequency of $44Hz$ for a stroke angle of roughly 60°. For the link parameters chosen, a simple kinematic analysis shows that piezo motion as small as $\pm0.25mm$ should provide as much as $\pm70^o$ of spar motion. This range of motion was not achieved pri-

marily due to alignment problems during construction and compliance in the flexures and cable.

This early experiment demonstrates that the single-crystal PZn-PT unimorph actuators, which are intended for the final product, can be fabricated at the desired scale (in the photo, the unimorph is $5mm \times 1mm \times 0.2mm$, with a $150\mu m$ thick PZn-PT plate bonded to a $50\mu m$ thick steel plate) and appear to provide the necessary actuation requirements. It should be noted that the PZn-PT in the photo was driven at only a third of the electric field which it can sustain so much larger displacements are achievable and the resonant frequency can be increased significantly by reducing the structural compliance. Unfortunately, the yield of operational actuators during fabrication has been very low, limiting the amount of experimentation that can be performed with them. The most current structure, described later, is driven by the Thunder^{TM} actuator, commercially-available from Face International Corporation.
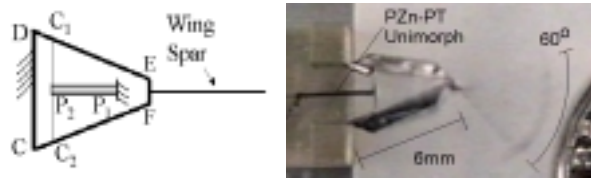

Figure 4: (a) Cable-driven four-bar; (b) Structure driven over 60° at $44Hz$ by PZn-PT unimorph

Figure 5(a) shows the current four-bar dimensions used. The actuation from the piezo unimorph goes through a 2-step amplification (notice that this design, in which link CF if fixed and link CD is driven, provides greater amplification to the spar motion than the original design of figure 4(a) in which link CD is fixed and links CF and DE are driven). An initial slider-crank mechanism, converts approximately linear motion at A into a rotation for link BC. The four-bar CDEF converts this small angular motion at the input link CD to a large rotation for the spar. The relation between the driving input δ and the spar output θ is shown in figure 5(b). The four-bar structure will be driven at high amplitudes where nonlinear effect need to be taken into account.

Figure 5(b) illustrates that an input actuation of $0.1mm$ is sufficient to get spar output motion of over 180°, for the ideal four-bar with pinjoints connecting adjacent links. In practice, roughly $0.5mm$ was required for this amount of output due to the joints being flexures, poor adhesion between the flexures and the links, etc.
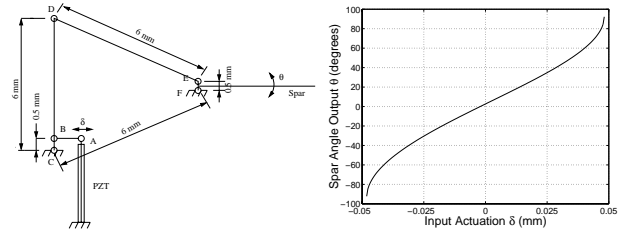

Figure 5: (a) Four-bar dimensions; (b) Ideal I/O characteristics.

### 2.1.3 2 DOF Wing Spar Kinematics
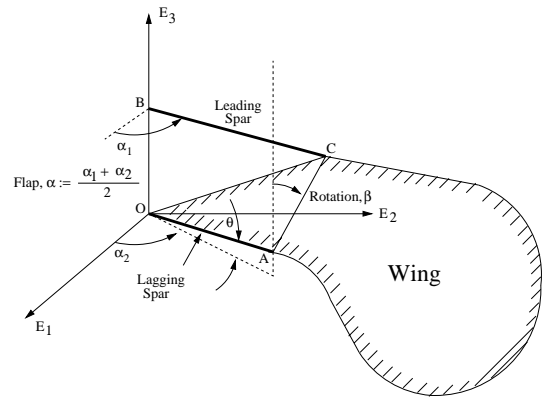
Figure 6: Kinematics of wing spar mechanism

The required flapping and rotation motions of a single wing can be achieved from the design of figure 6. The insect body frame is represented by $E_1 E_2 E_3$. It consists of two wing spars, OA and BC, each driven by two independently actuated fourbars. α_1 and α_2 are the actuated angles. The *leading spar* BC is restricted to move parallel to the $E_1 E_2$ plane. The *lagging spar* OA possesses a passive DOF, permitting movement out of plane $E_1 E_2$. The wing is coplanar to OAC. Simple flapping motion is achieved by setting $\alpha_1 = \alpha_2$ (*i.e.* spars are actuated in phase) so that $\theta = 0$. When $\alpha_1 \neq \alpha_2$, (*i.e.* the two spars are driven out of phase as shown in the figure), the lagging spar, OA moves up through an angle θ so that the distance AC is maintained constant. Because of this, a rigid wing can be connected as shown. The flapping angle α can be calculated as the mean of the actuated angles ($\alpha = \frac{\alpha_1 + \alpha_2}{2}$). For fixed spar lengths and a fixed spar separation distance, the rotation is only a function of the difference in the actuated angles (*i.e.*, $\beta = \beta(\alpha_2 - \alpha_1)$). For spars $4mm$ long and separated by $1mm$, a phase difference of only $+12^o$ is sufficient to cause a rotation of $\beta = +45^o$.

In this design, a large ratio of $\frac{OA}{AC}$ provides a large
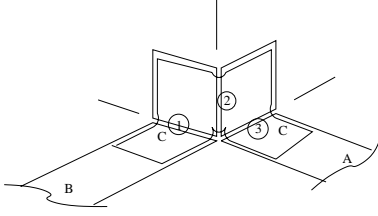
Figure 7: Spherical joint design

variation in the attack angle for a small phase difference $(\alpha_1 - \alpha_2)$ and the angle θ. This enables use of a flexural joint (or a revolute joint) between OA and AC. A spherical joint employed at C allows for all the motion required between AC and BC. The spherical joint consists of a series of 3 flexural joints between BC and AC as shown in figure 7.

The mechanism fabricated, shown in figure 8, was actuated using commercially available Thunder^{TM} actuators. Only 50° of flapping and 30° of rotation was achieved with this model but attaining the design goal of 140° of flapping and 90° of rotation is expected in the next design iteration by increasing the amplification for each four-bar mechanism.
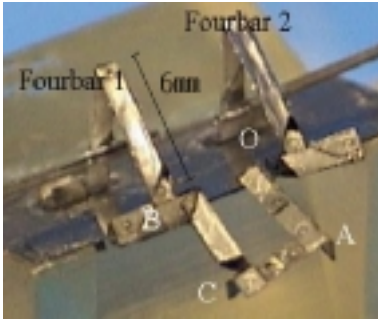

Figure 8: Photo of wing actuation mechanism (compare labels to figure 6).

2.1.4 Structural Dynamics

The wing mechanism should have low transmission losses, requiring a low damping ratio. In order to achieve a high resonant frequency, it should also be lightweight. Due to low actuator stiffness, care must be taken to avoid introducing unnecessary additional compliance into the transmission, which would effectively decrease the stiffness and hence the resonant frequency. In short, a low inertia, high stiffness mechanism with light damping is desired.

Fig 9 shows a simplified dynamic model of the four-bar. The Thunder^{TM} actuator is modeled as a mass-spring-damper system and the actuation is modeled as
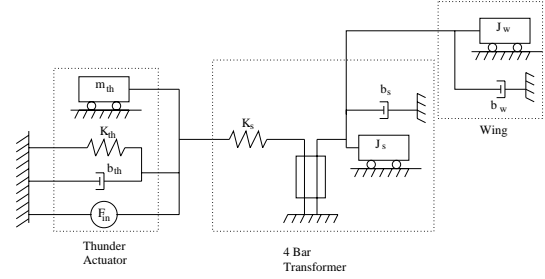

Figure 9: Fourbar Dynamics

a force input. The four-bar is treated as a linear, memoryless transmission element. The stiffness is lumped in series with the actuator while treating its inertia and damping as rotational terms acting in series with the load. As described in the following analysis, parameter identification was performed for the structural serial stiffness K_s, structural rotational inertia J_s, and structural rotational damping b_s.

A simplified second order model relating the force input to the angular output for the above system is:

$$\frac{\theta_o}{F_{in}} = \frac{N}{N^2(J_{th} + J_l)s^2 + N^2(b_{th} + b_s)s + K_{eq}}, \quad (4)$$

where, K_{eq}, the equivalent stiffness is given by:

$$K_{eq} = \frac{K_s K_{th}}{K_s + K_{th}}, \quad (5)$$

and the load inertia, J_l is given by:

$$J_l = J_s + J_w, \quad (6)$$

where the wing inertia J_w includes the inertia of the spars and the polyester wing itself.

The resonant frequency is given by:

$$\omega_r = \frac{1}{N}\sqrt{\frac{K_{eq}}{J_{th} + J_l}} \quad (7)$$

Measuring the variation in the resonant frequency with the load inertia therefore gives a means to determine the equivalent stiffness and inertia parameters of the structure. Similarly, fitting the frequency response with a second order system allows approximation of the damping coefficient ζ, and hence, the damping ratio $b = 2\zeta\omega_n J$.

2.1.5 Actuation Experimental Results

These two experiments were done first for the Thunder^{TM} actuator to characterize its parameters. The experiment was repeated with the four-bar structure and a load attached; accounting for the computed actuator parameters, the structural mass, stiffness and damping could also be identified.
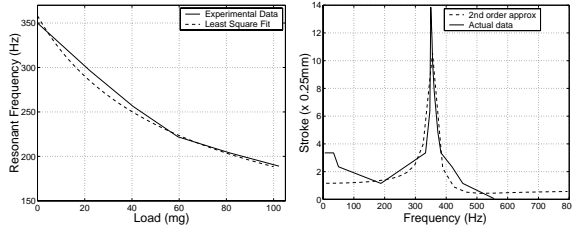
Figure 10: Thunder^{TM} actuator characterization: (a) Resonant frequency vs load; (b) Frequency response

From figure 10, the actuator parameters are determined as $J_{th} = 2.13 \times 10^{-11} kg \cdot m^2$, $K_{th} = 1936 N/m$, $\zeta = 2.66 \times 10^{-2}$, $\omega_n = 3.54 \times 10^2 rad/s$, and $b_{th} = 2\zeta\omega_n J_{th} = 2.53 \times 10^{-9} N \cdot m \cdot s/rad$.

Experiments with the four-bar structure attached to the actuator found the rotational inertia $J_s = 4.45 \times 10^{-11} kg \cdot m^2$, which is large relative to the expected wing inertia of $3.3 \times 10^{-11} kg \cdot m^2$; however, the current structure is still roughly 25% larger than the final target size. The rotational damping was calculated as $b_s = 6.2 \times 10^{-10} N \cdot m/(rad/s)$, which is also very low, permitting high efficiency; the power losses from this damping are estimated to be $0.6 mW$ per wing. The serial stiffness was found to be sufficiently high ($K_s > 1 kN/m$) that maintaining a high resonant frequency is not expected to be a problem.

2.2 Force Sensing

Measurement of wing forces is achieved using semiconductor strain gauges mounted directly on the wing spars. These measurements serve the dual purpose of initial off-line characterization of forces generated during wing motion and for feedback in the real-time wing control system.

The preliminary measurements described in this section were taken using a 5X scale model of the wing structure but the results are anticipated to scale well to the final target size.

Considering the wing spar as a rigid body, the moment M is directly proportional to the strain ϵ:

$$M = \frac{EI\epsilon}{z} \qquad (8)$$

where E is the wing elastic modulus, I is the cross-sectional moment of inertia and z is the distance of the gauge from the neutral axis. The force, F, is directly proportional to this moment:

$$F = \frac{M}{x - x_F} \qquad (9)$$

where the force acts at a distance x_F from the base of the spar. The unit x represents the distance from the fixed end of the cantilever to the point of measurement (the center of the gauge).

Initially, a single gauge was placed on the wing spar to measure the inertial and aerodynamic forces felt on the tip of the spar. The gauge was mounted to a polystyrene spar and positioned on the four-bar as in figure 11(a). The position of the gauge along the spar is crucial for the sensitivity of the measurements (see [2] and [6] for a discussion on force sensors and sensor placement). For a given force, the maximum moment, and thus the maximum strain is measured when the gauge is placed as close to the base of the cantilever as possible. This is clear from equation (9).
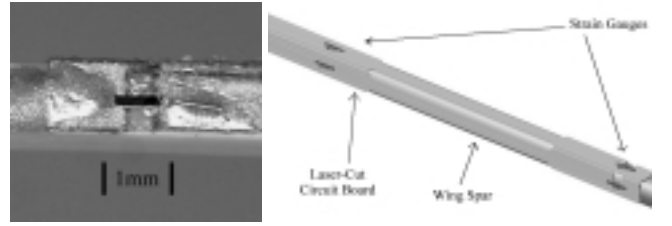
Figure 11: (a) $1mm$ strain gauge mounted on 5X polystyrene wing spar; (b) Dual-axis force sensors on wing spar.

Testing was done by fixing the base link of the four-bar and driving the side link with a VCA. Using an optical position sensor, closed-loop control of the VCA was performed with a PC equipped with a real-time ADC/DAC board (from Quanser Consulting). During a wing stroke, a force distribution develops along the wing spar. For a rigid body, this force distribution can be reduced to a single force acting at the center of force of the distribution. Using a pair of gauges located at two positions along the wing spar, as shown in figure 11(b), both the equivalent force F_{eq} and the center of force x_{eq} can be solved from the system of equations:

$$M_i = F_{eq}(x_i - x_{eq}) \qquad (10)$$

where M_i and x_i ($i = 1, 2$) are the measured moment and gauge position along the spar, respectively. Using a dual-axis force sensor in which the gauges are mounted orthogonal to each other, the force can be resolved into two components orthogonal to the wing spar. The component which is also orthogonal to the stroke plane is related to the lift force while the other component is related to the drag force.

The sensitivity of the system at the 5X scale was measured to be less than $1mN$, based on $E = 3GPa$, $I = 8 \times 10^{-14} m^4$, $z = 0.5mm$, and a minimum readable strain from the gauges of $0.1\mu\epsilon$. This gives a usable resolution with off-the-shelf strain gauge am-

plifiers. The calculated sensitivity at the final size is roughly $100\mu N$.

A 5X wing spar was construced from a $1mm$ square wing spar, $50mm$ long with a laser-cut flexible circuit board mounted on two adjacent faces of the spar. The strain gauges were fixed and soldered to the board. Although the gauges are small enough to use at the final size, the wiring becomes increasingly difficult. To alleviate this, a wing fabricated using MEMS technology is being pursued, with built-in strain gauges and amplification circuitry.

2.2.1 Sensing Experimental Results

The 5X scale structure had a mylar wing attached which could be rotated to change the attack angle. The wing was driven at $16Hz$ with a stroke amplitude of 30°. The raw data extracted from the force sensors consists of both the spar inertial forces and the wing aerodynamic forces. This total force is not, in itself, useful but the inertial force can be determined separately, by placing an equivalent point mass at the end of a massless cantilever and repeating the experiment. The aerodynamic force can then be determined as the difference between the total force and the inertial force. Experimental determination of the inertial forces was done by orienting the wing orthogonal to the stroke plane and is shown in figure 12. It is interesting to note that Dickinson *et al* assume that the location of the center of force is constant in [4] and this is roughly observed to be true in figure 12(b).
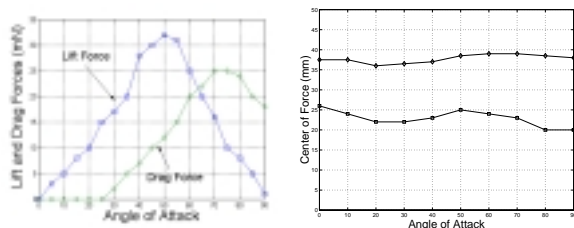
Figure 12: (a) Lift and drag forces measured vs. attack angle; (b) Centers of force for lift and drag.

2.3 Power Transmission

The MFI needs to be very lightweight, precluding the use of conventional batteries. As shown in the block diagram in figure 13, it is anticipated that a solar panel array and a miniature Li battery should provide $13mW$ of power. Using the charge recovery system described in this section, an overall power transfer efficiency greater than 75% results in $10mW$ of mechanical energy to the wings.
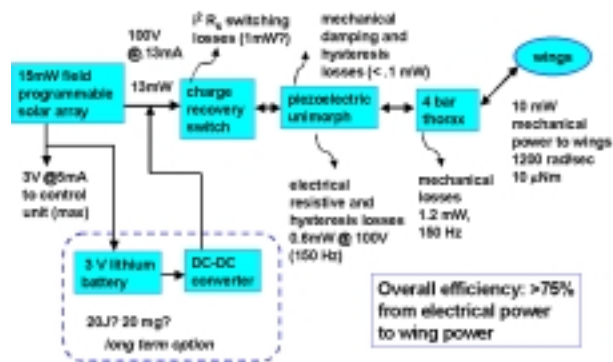
Figure 13: Power efficiency

Piezoelectric actuators exhibit parasitic capacitance and many problematic power issues arise from charging or discharging such a capacitor by means of a constant voltage source and a switching stage. In ([1]), Athas *et al* showed that efficient capacitors can be charged efficiently with a voltage ramp (*i.e.* a constant current source) but circuits for generating such an input tend to dissipate too much energy in the power supply itself, even without a load. The basic operation of a simple charge recovery system is shown in figure 14. This circuit introduces an inductor into the system to take advantage of the oscillating nature of LC circuits.
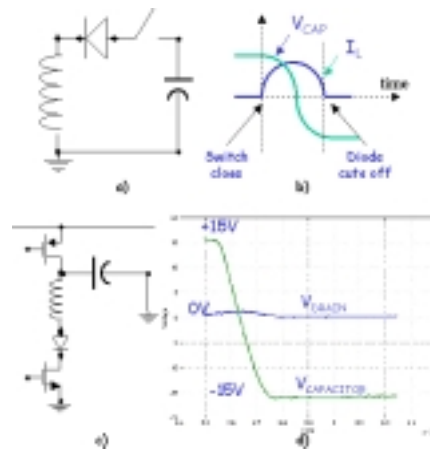
Figure 14: (a) LC oscillating circuit when current is positive; (b) inductor current and capacitor voltage vs. time; (c) implemented circuit; and (d) acquired waveforms from circuit.

Figure 15 shows the electrical equivalent model of the entire system, combining the power supply, switching stage and the piezoelectric actuator. C_{stiff} represents the piezoelectric mechanical stiffness while L_{wing} and R_{damp} are the wing inertia and damping, respec-

tively (piezoelectric inertia and damping are negligible compared with the wing parameters). The four-bar mechanism is modelled as an ideal transformer with a turns ratio T. The system can mostly be considered as a linear, time-invariant (LTI) system. The only nonlinear element is the hysteretic capacitor that, together with the linear capacitor, models the parasitic Capacitance of the piezoelectric actuator [8].
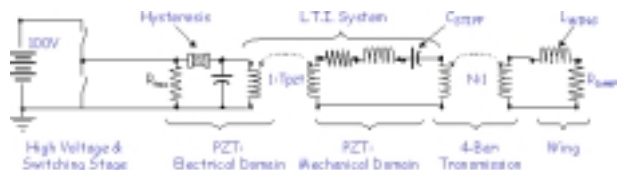

Figure 15: Electrical equivalent of overall system.

3 Wing Control Issues

There are some interesting control problems for the MFI. In this section, issues related only to low-level control are discussed in which tracking of a wing force or position trajectory is desired.

One problem that needs to be addressed is that the wings will be driven near resonance, a mode which is typically purposely suppressed in most control applications. As a result, the phase lag between the input actuation signal and the motion is 90°, effectively introducing a "time delay" into the control. Thus, there are no ways to control the position of the wing except on a stroke-by-stroke basis; there is evidence to suggest this is true even for biological flying insects. Since the forces measured by the strain gauges are mostly inertial, it is possible to use these signals as a feedback for a control system.

The switching controller described in section 2.3 adds complexity to the problem by making it a hybrid system. Nonlinearity, time-varying terms are introduced by the piezoelectric material and the unknown aerodynamic drag.

Robustness will be an important concern and a stochastic models of the noise and disturbances which may be encountered (*e.g.,* measurement noise, wind gusts, *etc.*) need to be developed.

Figure 16 shows a block diagram realization for a wing controller. The control is based upon a desired force signal, generated on a stroke-by-stroke basis (or half-stroke-by-half-stroke basis). The reference force signal, generated by the high level MFI controller, is compared to the actual force measured by the wing spar force sensors. The raw force measured by the wing spar sensors consists of the combination of inertial and
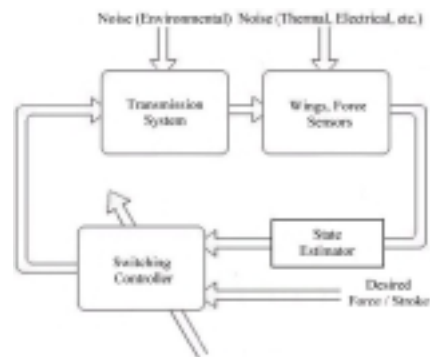

Figure 16: Wing controller

aerodynamic forces. The force measured by the sensor, F, is modeled by the expression:

$$F = m_s\ddot{x} + b_w(x, \dot{x}, t) + k_s x \qquad (11)$$

where m_s is the spar mass, k_s is the spar stiffness, and $b_w(\cdot, \cdot, t)$ is the nonlinear, time-varying wing damping. For the control experiment in this paper, this damping is taken to be LTI (*i.e.,* $b_w(x, \dot{x}, t) = b_w\dot{x}$).

3.1 Example Wing Trajectory

The wing trajectory of an insect is characterized by numerous parameters including stroke angle, rotation angle, attack angle, frequency, upstroke-to-downstroke time ratio, dorsal and ventral flip timing and deviation from the stroke plane (in the current MFI wing design, this parameter cannot be controlled).

An example wing trajectory was generated using the following parameters: stroke of $\pm 70^o$, rotation of $\pm 45^o$, 30° angle of attack, frequency of $f = 1/T = 150Hz$, downstroke time of $0.7T$, upstroke time of $0.3T$, and $\pm 0.1T$ start and end of the dorsal and ventral flip timing. The resulting kinematic flapping and rotation angles are shown as a function of time in Figure 17(a). Solving the inverse kinematic relations gives the necessary unimorph displacements to generate the desired trajectory (see figure 17(b)).

For the MFI, force control is more apt than position control because of the need to generate lift forces. A simple sawtooth signal was selected as a force reference trajectory for the 5X model. This signal is an interesting one to track because of the asymmetry and the high frequency components. A simple PD controller was employed using this trajectory and the force signal to generate the results in figure 18. Similar experiments need to be performed on an instrumented final-sized structure once it has been fabricated.
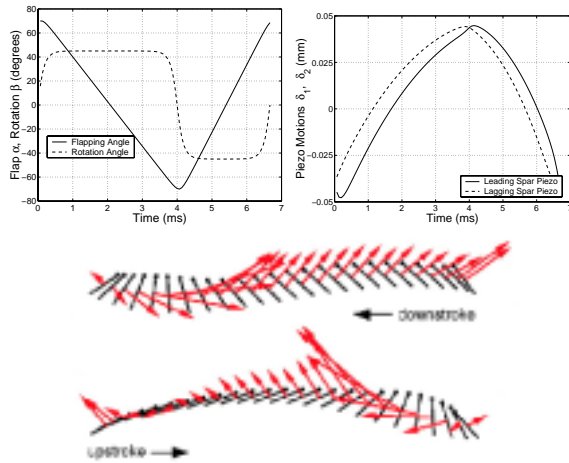
Figure 17: (a) Desired flapping and rotation motions; (b) Required unimorph displacements; (c) Wing chord positions separated by constant time intervals and instantaneous forces.
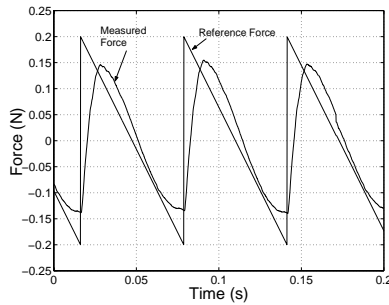

Figure 18: Force tracking experiment.

4   Discussion

This paper presents recent progress on the UC Berkeley MFI project, specifically related to the actuation (structure, kinematics, *etc.*), sensing, power transmission and control. In the near term, the thorax structure described in section 2.1.3 will be constructed at final size and instrumented with the strain gauges described in section 2.2. Various control strategies will be employed and compared for their force generation and tracking capabilities.

Acknowledgments

References

[1] W.C. Athas, J.G. Koller, and L.J. Svensson. An energy efficient CMOS line driver using adiabatic switching. In *Proc of 4th Great Lakes Symposium on VLSI*, Notre Dame, IN, Mar 4-5 1994.

[2] A. Bicchi, A. Caiti, and D. Prattichizzo. Optimal design of a multi-axis force/torque sensor. In *Proc of IEEE Intl Conf on Decision and Control*, Phoenix, AZ, Dec 1999.

[3] A. Cox, E. Garcia, and M. Goldfarb. Actuator development for a flapping microrobotic mav. In *SPIE Microrobotics Symp*, pages 102–108, Boston, MA, Nov 1998.

[4] M.H. Dickinson, F-O. Lehmann, and S.P. Sane. Wing rotation and the aerodynamic basis of insect flight. *Science*, 284:1954–1960, June 1999.

[5] C.P. Ellington, C. van den Berg, A.P. Willmot, and A.L.R. Thomas. Leading edge vortices in insect flight. *Nature*, 384:626–630, December 1996.

[6] S. Fahlbusch and S. Fatikow. Force sensing in microrobotic systems - an overview. In *Proc of IEEE Intl Conf on Electronics, Circuits and Systems*, pages 259–262, Lisbon, Portugal, Sept 1998.

[7] R.S. Fearing, K.H. Chiang, M.H. Dickinson, D.L. Pick, M. Sitti, and J. Yan. Wing transmission for a micromechanical flying insect. In *Proc of IEEE Intl Conf on Robotics and Automation*, pages 1509–1516, San Francisco, CA, April 2000.

[8] M. Goldfarb and N. Celanovic. Modelling piezoelectric stack actuator for control of micromanipulation. *IEEE Control Systems Magazine*, 17:69–79, June 1997.

[9] Y. Kubo, I. Shimoyama, T. Kaneda, and H. Miura. Study on wings of flying microrobots. In *Proc of IEEE Intl Conf on Robotics and Automation*, pages 834–839, San Diego, CA, May 1994.

[10] B. Motazed, D. Vos, and M. Drela. Aerodynamics and flight control design for hovering MAVs. In *Proc of Amer Control Conf*, Philadelphia, PA, June 1998.

[11] T.N. Pornsin-Sirirak, S.W. Lee, H. Nassef, J. Grasmeyer, Y.C. Tai, C.M. Ho, and M. Keennon. MEMS wing technology for a battery-powered ornithopter. In *Proc. of IEEE 13th Annual Intl Conf on MEMS*, pages 799–804, Piscataway, NJ, Jan 2000.

[12] E. Shimada, J.A. Thompson, J. Yan, R.J. Wood, and R.S. Fearing. Prototyping millirobots using dextrous microassembly and folding. In *to appear, Symp on Microrobotics ASME Intl Mech Eng Cong and Expo*, Orlando, FL, Nov 5-10 2000.

[13] I. Shimoyama, H. Miura, K. Suzuki, and Y. Ezura. Insect-like microrobots with external skeletons. *IEEE Control Systems Magazine*, 13:37–41, February 1993.

[14] K. Suzuki, I. Shimoyama, and H. Miura. Insect-model based microrobot with elastic hinges. *IEEE MEMS*, 3:4–9, March 1994.